Journal of Alloys and Compounds 753 (2018) 412–421

Contents lists available at ScienceDirect

Journal of Alloys and Compounds

journal homepage: http://www.elsevier.com/locate/jalcom

Microstructure of equiatomic and non-equiatomic Ti-Nb-Ta-Zr-Mo high-entropy alloys for metallic biomaterials

Takeshi Nagase [a, b], Mitsuharu Todai [c], Takao Hori [a], Takayoshi Nakano [a, *]

[a] Division of Materials and Manufacturing Science, Graduate School of Engineering, Osaka University, 2-1 Yamadaoka, Suita, Osaka 565-0871, Japan
[b] Research Center for Ultra-High Voltage Electron Microscopy, Osaka University, 7-1, Mihogaoka, Ibaraki, Osaka 567-0047, Japan
[c] Department of Environmental Materials Engineering, National Institute of Technology, Niihama College, 7-1 Yagumo-cho Niihama, Ehime 792-8580, Japan

ARTICLE INFO

Article history:
Received 29 December 2017
Received in revised form
5 April 2018
Accepted 7 April 2018
Available online 19 April 2018

Keywords:
Biomaterial
High-entropy alloy
Microstructure
Solidification
Thermodynamic calculation

ABSTRACT

The microstructures of equiatomic TiNbTaZrMo ($Ti_{20}Nb_{20}Ta_{20}Zr_{20}Mo_{20}$—subscript numerals denote at.%) and non-equiatomic $Ti_{2.6}NbTaZrMo$ ($Ti_{39.4}Nb_{15.2}Ta_{15.2}Zr_{15.2}Mo_{15.2}$) high-entropy alloys (HEAs) were investigated for use in metallic biomaterials, and discussed based on their thermodynamics. Equiaxial dendrite structures were observed in the as-cast specimens. Ta, Nb, and Mo were abundant in the main dendrite phase with a body centered cubic (bcc) structure, while Ti and Zr showed a tendency to be abundant in the inter-dendrite region with a bcc structure. The distribution of the constituent elements can be explained through the distribution coefficients during solidification estimated using thermodynamic calculations. The thermodynamic calculations focusing on the solidification process were effective not only for the evaluation of the solidification microstructure, but also for the design of Ti-Nb-Ta-Zr-Mo-based HEAs. The non-equiatomic $Ti_{2.6}NbTaZrMo$ HEA ($Ti_{39.4}Nb_{15.2}Ta_{15.2}Zr_{15.2}Mo_{15.2}$) was designed based on thermodynamic calculations and the solidification microstructure was studied.

1. Introduction

There is a need for a new generation of metallic biomaterials with superior biocompatibility and mechanical properties to meet future demands of the medical field. Recently, a new class of structural materials—high-entropy alloys (HEAs)—was developed [1–7]. We developed an equiatomic TiNbTaZrMo HEA for metallic biomaterials based on the empirical alloy parameters for HEAs (an alloy with an atomic ratio of Ti:Zr:Nb:Ta:Mo = 1:1:1:1:1; the alloy is referred to as TiNbTaZrMo herein ($Ti_{20}Nb_{20}Ta_{20}Zr_{20}Mo_{20}$ [at.%])) [8]. Wang and Xu also reported the use of equiatomic TiNbTaZrMo ($Ti_{20}Nb_{20}Ta_{20}Zr_{20}Mo_{20}$) for orthopedic implants [9]. This novel equiatomic HEA shows superior biocompatibility compared to that of pure Ti and mechanical properties, such as yield stress, that are superior to those of the Ti-6Al-4V alloy. It also shows superior workability in spite of its significantly higher strength. It was found that the biocompatibility and mechanical properties could be modified by annealing, as shown in the reference data [8], and this may be related to changes in the microstructure caused by annealing. However, the microstructures of an as-cast ingot of equiatomic TiNbTaZrMo ($Ti_{20}Nb_{20}Ta_{20}Zr_{20}Mo_{20}$) and annealed specimens have not been studied in detail, and the relationship between the experimentally observed microstructure and the thermodynamic calculation results has not been discussed. In the present study, the microstructures of as-cast and annealed equiatomic TiNbTaZrMo ($Ti_{20}Nb_{20}Ta_{20}Zr_{20}Mo_{20}$) were investigated in detail. The microstructures were studied and correlated with the results of thermodynamic calculations. Furthermore, a non-equiatomic $Ti_{2.6}NbTaZrMo$ ($Ti_{39.4}Nb_{15.2}Ta_{15.2}Zr_{15.2}Mo_{15.2}$) HEA was designed based on thermodynamic calculations.

2. Materials and methods

The nominal compositions of the alloys investigated in the present study—the equiatomic quaternary TiNbTaZr ($Ti_{25}Nb_{25}Ta_{25}Zr_{25}$) alloy, equiatomic five-component TiNbTaZrMo HEA, and non-equiatomic five-component Ti-Zr-Nb-Ta-Mo HEAs—are summarized in Table 1. Arc-melted ingots were prepared by mixing lumps of the pure elements. Ti chips (purity = 3 N), Nb granules (purity = 3 N, 2–5 mm), Ta granules (purity = 3 N, 2–5 mm), and Zr wire-cut products (purity = 3 N, 5ϕ × 5 mm) were supplied by Mitsuwa Chemicals Co. Ltd., Japan [10]. Zirconium sponge (purity = 2 N) was also used for ingot preparation and was obtained

* Corresponding author.
E-mail address: nakano@mat.eng.osaka-u.ac.jp (T. Nakano).

https://doi.org/10.1016/j.jallcom.2018.04.082

Table 1
Nominal compositions of equiatomic TiNbTaZr ($Ti_{25}Nb_{25}Ta_{25}Zr_{25}$—subscript numerals denote at.%) alloy and equiatomic TiNbTaZrMo ($Ti_{20}Nb_{20}Ta_{20}Zr_{20}Mo_{20}$) and non-equiatomic Ti-Zr-Nb-Ta-Mo HEAs.

Alloys	Ti	Nb	Ta	Zr	Mo
TiNbTaZr	25.0	25.0	25.0	25.0	
TiNbTaZrMo	20.0	20.0	20.0	20.0	20.0
$Ti_{2.6}$NbTaZrMo	39.4	15.2	15.2	15.2	15.2
$TiNbTa_{0.2}$ZrMo	23.8	23.8	4.8	23.8	23.8
$TiNbTaZr_{2.6}$Mo	15.2	15.2	15.2	39.4	15.2
$TiNbTaZrMo_{0.2}$	23.8	23.8	23.8	23.8	4.8

from Nilaco Co. Ltd., Japan [11]. Mo shots (purity = 3 N, 2 mm) supplied by Rare Metallic Co. Ltd., Japan [12] and Mo bars (purity = 3 N, 5ϕ × 1000 mm) supplied by Osaka Asahi Ltd., Japan [13] were used. To achieve a homogeneous distribution of constituent elements in the alloy, the alloy was melted more than 10 times and maintained in a liquid state for approximately 300 s during each melting event. The cooling rate during the arc melting process was approximately 10^3 K^{-1} [14]. The solidification microstructures of the arc-melted ingots of equiatomic TiNbTaZrMo ($Ti_{20}Nb_{20}Ta_{20}Zr_{20}Mo_{20}$) and the non-equiatomic $Ti_{2.6}$NbTaZrMo HEA (the alloy with an atomic ratio of Ti:Zr:Nb:Ta:Mo = 2.6:1:1:1:1, $Ti_{39.4}Nb_{15.2}Ta_{15.2}Zr_{15.2}Mo_{15.2}$—subscript numerals denote at.%) were investigated. To clarify the annealing-induced structural changes, the microstructure of equiatomic TiNbTaZrMo ($Ti_{20}Nb_{20}Ta_{20}Zr_{20}Mo_{20}$) annealed at 1273 K for 168 h was also investigated. X-ray diffraction (XRD) analysis was performed using a Philips X-pert Pro (PANalytical, Japan) and a Rigaku RINT-2500 (Rigaku, Japan) with Cu-K_α radiation to identify the constituent phases. The microstructure was examined using optical microscopy (OM), scanning electron microscopy (SEM) using a field emission scanning electron microscope (JSM-6500F, JEOL, Japan), electron probe microanalysis (EPMA) with wavelength-dispersive spectroscopy (WDS; JXA-8800R, JEOL, Japan), and transmission electron microscopy (TEM; H-800, Hitachi, Japan). The thermodynamic calculations for the Ti-Nb-Ta-Zr and Ti-Nb-Ta-Zr-Mo alloys were performed with FactSage (ver. 6.4) using the thermodynamic databases for alloy systems from Scientific Group Thermodata Europe (SGTE) 2007 [15]. The database was not constructed by a simple regular solid-solution model with heat of mixing estimated by the Miedema model; however, the excess Gibbs energy of mixing in the liquid phase was described by the Redlich-Kister-Muggianu polynomial expression under a regular solution model. Critical assessment of the polynomial parameters was performed in order to reproduce most of the available experimental data on thermodynamic properties and phase equilibria.

3. Results

Fig. 1 shows the XRD patterns of the as-cast and annealed equiatomic TiNbTaZrMo ($Ti_{20}Nb_{20}Ta_{20}Zr_{20}Mo_{20}$) [8]. Two peaks (indicated by ● and ○) can be seen for the as-cast state. The constituent phases in the as-cast equiatomic TiNbTaZrMo ($Ti_{20}Nb_{20}Ta_{20}Zr_{20}Mo_{20}$) were identified as a main body centered cubic (bcc) solid-solution phase with a lattice constant of 0.325 nm (●) and a minor bcc phase with a lattice constant of 0.333 nm (○). The XRD patterns did not indicate the formation of any intermetallic compound phase or bcc-based ordered phase. Annealing did not lead to the decomposition of bcc solid-solution phases to other phases or the formation of intermetallic compounds in equiatomic TiNbTaZrMo ($Ti_{20}Nb_{20}Ta_{20}Zr_{20}Mo_{20}$), and caused only a slight change in the minor bcc phase (●). The peak positions of the minor bcc phase were shifted to lower angles, and the ratio of the peak

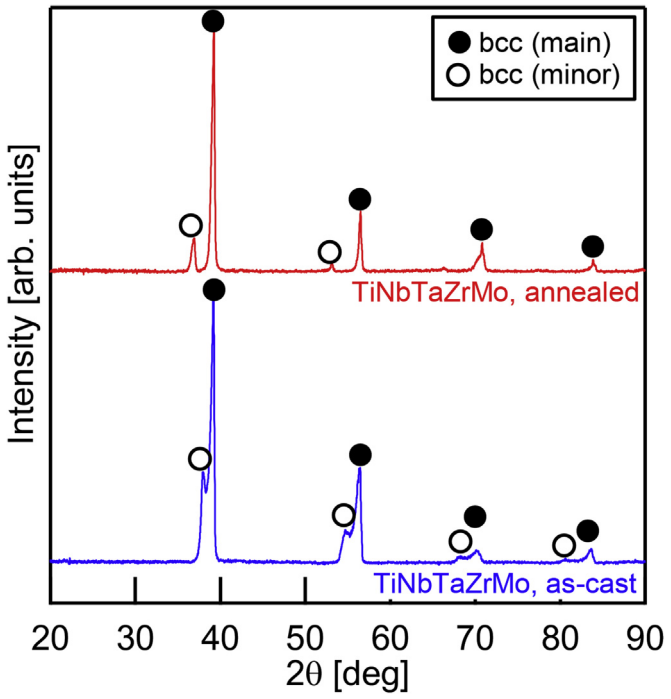

Fig. 1. XRD patterns of equiatomic TiNbTaZrMo ($Ti_{20}Nb_{20}Ta_{20}Zr_{20}Mo_{20}$) HEA as cast and annealed at 1273 K for 168 h.

intensity of the minor bcc phase (●) to that of the main bcc phase (○) decreased. The bcc solid-solution phase shows high phase stability in equiatomic TiNbTaZrMo ($Ti_{20}Nb_{20}Ta_{20}Zr_{20}Mo_{20}$).

Fig. 2 shows the SEM back-scattering electron (BSE) image of equiatomic TiNbTaZrMo ($Ti_{20}Nb_{20}Ta_{20}Zr_{20}Mo_{20}$). An equiaxial fine dendrite structure was observed in the as-cast equiatomic TiNbTaZrMo ($Ti_{20}Nb_{20}Ta_{20}Zr_{20}Mo_{20}$) (Fig. 2a), which was independent of the sample position in the ingots [8]. A dendrite structure indicates redistribution of the constituent elements during solidification, which results in the formation of a mixture of a main dendrite phase (with white contrast; index A) and a minor phase of the inter-dendrite region (with dark gray contrast; index B) as shown in the magnified image. The inter-dendrite region (B) appeared to be a single phase. The microstructure of equiatomic TiNbTaZrMo ($Ti_{20}Nb_{20}Ta_{20}Zr_{20}Mo_{20}$) in the as-cast state was investigated in detail using TEM in a previous study [8], and the primary findings were as follows: (1) no crystalline precipitates were observed in bright-field TEM images, and (2) the diffraction spots based on a B2 ordering phase and those corresponding to the ω phase were not observed in the TEM electron diffraction images. These results indicated the formation of a bcc solid-solution phase without significant chemical ordering or inclusions in the as-cast equiatomic TiNbTaZrMo ($Ti_{20}Nb_{20}Ta_{20}Zr_{20}Mo_{20}$). Coarsening of the main dendrite phase with white contrast can be seen in the annealed equiatomic TiNbTaZrMo ($Ti_{20}Nb_{20}Ta_{20}Zr_{20}Mo_{20}$) (Fig. 2b). The coarse dendrite showed an inhomogeneous contrast. The central area at the coarse dendrite (index C) shows a light gray contrast, while the surrounding region at the coarse dendrite (index D)—which lies next to the inter-dendrite region with the black contrast (index F)—shows a white-gray contrast. One can notice that a film-like phase (index E) with a dark gray contrast was embedded in the inter-dendrite region (F). Fig. 3 shows the elemental map obtained using EPMA-WDS, and Table 2 shows the results of atomic composition analysis. The main dendrite (A) was enriched with Ta (Fig. 3a3), whereas Ti and Zr were concentrated in

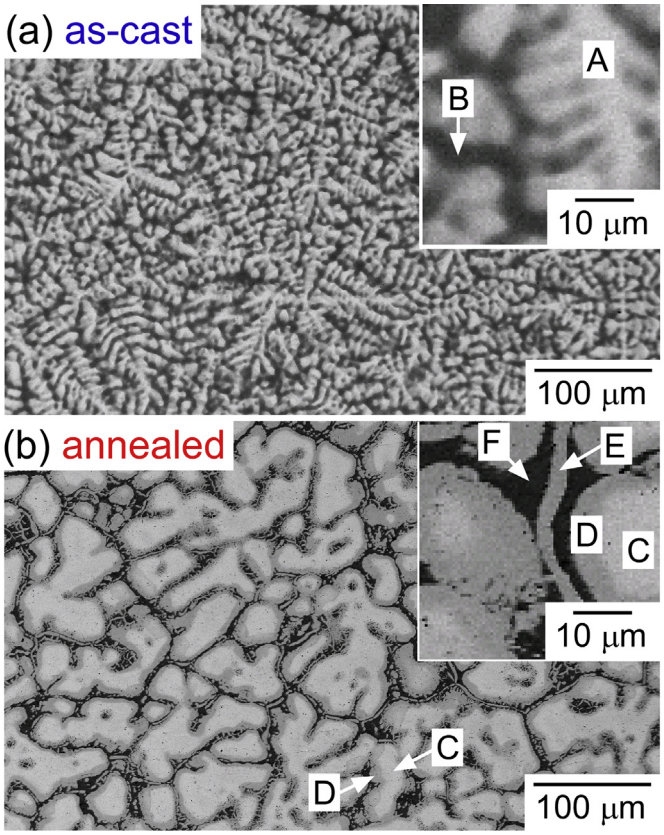

Fig. 2. SEM-BSE images of equiatomic TiNbTaZrMo ($Ti_{20}Nb_{20}Ta_{20}Zr_{20}Mo_{20}$) HEA: (a) as-cast and (b) annealed at 1273 K for 168 h.

the inter-dendrite (B) (Fig. 3a2, 3a4). Table 1a indicates that region A was enriched with Ta, Nb, and Mo, whereas Ti and Zr were concentrated in region B. The main dendrite (A) and inter-dendrite (B) regions in the as-cast equiatomic TiNbTaZrMo ($Ti_{20}Nb_{20}Ta_{20}Zr_{20}Mo_{20}$) both contained all constituent elements, which led to the formation of multicomponent solid-solution phases. The microstructure and the distribution of the constituent elements in equiatomic TiNbTaZrMo ($Ti_{20}Nb_{20}Ta_{20}Zr_{20}Mo_{20}$) changed after it was annealed. Ta was abundant in the coarse dendrite regions (C and D), as shown in Fig. 3b3. In contrast, Zr was concentrated in the inter-dendrite region (F), while Ti showed a tendency to be contained in both the inter-dendrite region (F) and the region surrounding the coarse dendrite (D). The EPMA-WDS analysis results for the annealed equiatomic TiNbTaZrMo ($Ti_{20}Nb_{20}Ta_{20}Zr_{20}Mo_{20}$) are shown in Table 2b. The central region of the coarse dendrite (C), the region surrounding the coarse dendrite (D), and the film-shaped phase (E) embedded in the inter-dendrite region show the following tendencies: (1) they contained all constituent elements, (2) Zr was diluted from the nominal composition, and (3) the chemical composition of the coarse dendrite was not homogeneous. Ta was abundant in the central area of the coarse dendrite, while Ti showed the opposite tendency. No significant differences were observed in the Nb, Mo, and Zr contents in the central region and the region surrounding the coarse dendrite. One can notice that Zr was abundant in the inter-dendrite region (F), and the enrichment in Zr was encouraged by annealing. The elemental distributions in the annealed specimens correspond partially to the distributions in the as-cast specimens, indicating that the microstructures in the annealed specimens were affected by segregation during solidification. The lattice constants estimated using Vegard's law [16] and the WDS analysis results are summarized in Table 3. The difference between the lattice constants of the central region (C) and the region (D) surrounding the coarse dendrite is insignificantly small in spite of the different chemical compositions. One can notice that the values of the lattice constant of the main dendrite (A) in the as-cast specimen and those of regions C, D, and E in the annealed equiatomic TiNbTaZrMo ($Ti_{20}Nb_{20}Ta_{20}Zr_{20}Mo_{20}$) are similar. The thermal equilibrium state in equiatomic TiNbTaZrMo ($Ti_{20}Nb_{20}Ta_{20}Zr_{20}Mo_{20}$) was not clarified. However, the appearance of bcc phases with different compositions and similar lattice constants implies that the constituent elements in equiatomic TiNbTaZrMo ($Ti_{20}Nb_{20}Ta_{20}Zr_{20}Mo_{20}$) may be redistributed by minimizing the lattice strain.

Fig. 4 shows pseudo-binary phase diagrams focusing on the liquidus and solidus temperatures of Ti-Nb-Ta-Zr-Mo alloys, which were estimated based on thermodynamic calculations considering a single liquid phase and a single solid-solution phase with a bcc structure: (a) MoNbTaZr-Ti, (b) TiMoTaZr-Nb, (c) TiNbMoZr-Ta, (d) TiNbTaMo-Zr, and (e) TiNbTaZr-Mo. It should be emphasized here that the thermal equilibrium state cannot be discussed based on the data presented in Fig. 4 alone; however, the melting of the bcc solid-solution phase and the solidification of the liquid to form the bcc solid-solution phase can be discussed. The liquidus and solidus temperatures of the equiatomic TiNbTaZrMo ($Ti_{20}Nb_{20}Ta_{20}Zr_{20}Mo_{20}$) were estimated to be 2600 and 2433 K, respectively. The hypothetical melting temperature, which was calculated from the rule of mixtures of the melting temperatures of the pure elements, was 2592 K for equiatomic TiNbTaZrMo ($Ti_{20}Nb_{20}Ta_{20}Zr_{20}Mo_{20}$). The similarity between the liquidus temperature estimated through thermodynamic calculations and the hypothetical melting temperature implies that the mixing of the constituent elements is not effective in stabilizing the liquid state with the decrease in the melting temperature by alloying. The predicted liquidus and solidus temperatures of equiatomic TiNbTaZrMo ($Ti_{20}Nb_{20}Ta_{20}Zr_{20}Mo_{20}$) are too high to be evaluated experimentally using differential thermal analysis (DTA) or differential scanning calorimetry (DSC). The DTA curves of the as-cast equiatomic TiNbTaZrMo ($Ti_{20}Nb_{20}Ta_{20}Zr_{20}Mo_{20}$), up to a temperature of 1773 K, are shown in Fig. S1 in the supplementary material; the occurrence of melting was not detected below 1773 K. Higher-temperature DTA measurements, focusing on melting and solidification, are difficult owing to the limitations of the instrument and increased reactivity between the sample holders and the Ti in the alloys. Thus, thermodynamic calculations were used to estimate the liquidus and solidus temperatures of the Ti-Nb-Ta-Zr-Mo-based HEAs. The MoNbTaZr-Ti alloy phase diagram (Fig. 4a) shows that both the liquidus and solidus temperatures of the Ti-Nb-Ta-Zr-Mo alloys decreased monotonously with an increase in the Ti content. Increases in the Ti and Zr contents led to decreases in the liquidus and solidus temperatures of the Ti-Nb-Ta-Zr-Mo alloys (Fig. 4a and d). In contrast, the liquidus and solidus temperatures increased with increasing Mo and Ta contents in the Ti-Nb-Ta-Zr-Mo alloys (Fig. 4c and e). The liquidus and solidus temperatures of the Ti-Nb-Ta-Zr-Mo alloys showed a tendency to increase monotonously with increases in the contents of high-melting-temperature elements (i.e., Mo and Ta) and to decrease with increases in the contents of low-melting-temperature elements (i.e., Ti and Zr). The degree of the changes in the liquidus and solidus temperatures of the Ti-Nb-Ta-Zr-Mo alloys due to changes in the Nb content is smaller than that due to changes in the contents of the other elements (Fig. 4b), and this is related to the similarity of the melting temperature of Nb (2750 K) to the liquidus temperature of equiatomic TiNbTaZrMo ($Ti_{20}Nb_{20}Ta_{20}Zr_{20}Mo_{20}$). The liquidus slopes ($m_L$) of equiatomic TiNbTaZrMo ($Ti_{20}Nb_{20}Ta_{20}Zr_{20}Mo_{20}$), estimated using the liquidus lines

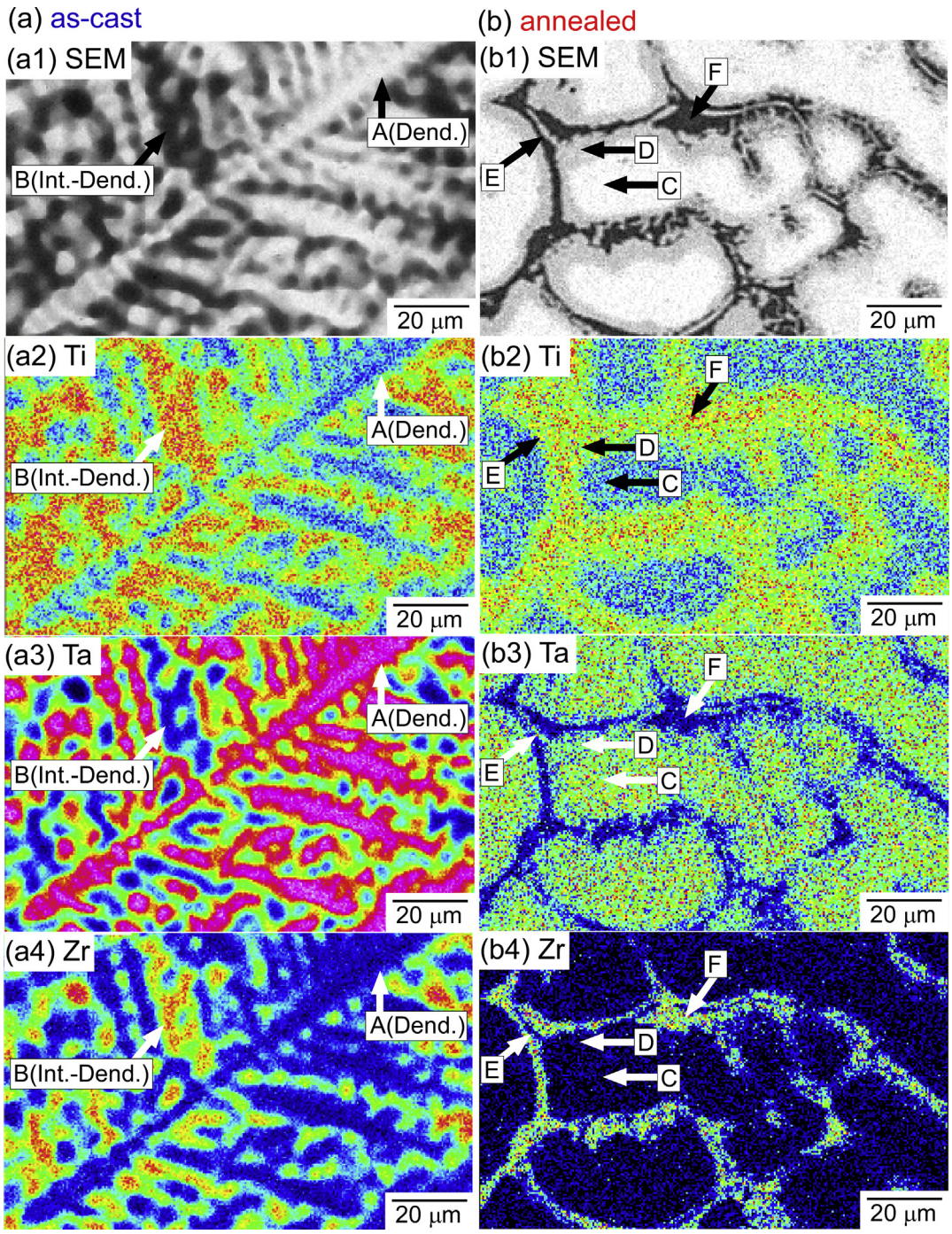

Fig. 3. EPMA elemental maps of (a1–a4) as-cast equiatomic TiNbTaZrMo ($Ti_{20}Nb_{20}Ta_{20}Zr_{20}Mo_{20}$) HEA and (b1–b4) annealed at 1273 K for 168 h: (a1), (b1) SEM-BSE images; (a2), (b2) Ti; (a3), (b3) Ta; (a4), (b4) Zr.

obtained from the thermodynamic calculations, were $m_{L-Ti} = -8.4$ K/x for $(Mo_{0.25}Nb_{0.25}Ta_{0.25}Zr_{0.25})_{100-x}Ti_x$, $m_{L-Nb} = +0.5$ K/x for $(Ti_{0.25}Mo_{0.25}Ta_{0.25}Zr_{0.25})_{100-x}Nb_x$, $m_{L-Ta} = +8.8$ K/x for $(Ti_{0.25}Nb_{0.25}Mo_{0.25}Zr_{0.25})_{100-x}Ta_x$, $m_{L-Zr} = -6.2$ K/x for $(Ti_{0.25}Nb_{0.25}Ta_{0.25}Mo_{0.25})_{100-x}Zr_x$, and $m_{L-Mo} = +5.2$ K/x for $(Ti_{0.25}Nb_{0.25}Ta_{0.25}Zr_{0.25})_{100-x}Mo_x$. These values corresponded to the difference between the melting temperature of the pure element (T_m) and the liquidus temperature of equiatomic TiNbTaZrMo ($Ti_{20}Nb_{20}Ta_{20}Zr_{20}Mo_{20}$) ($T_L$), with $T_{m-Ti} - T_L = -659$ K, $T_{m-Nb} - T_L = 150$ K, $T_{m-Ta} - T_L = 690$ K, $T_{m-Zr} - T_L = -472$ K, and $T_{m-Mo} - T_L = 296$ K, because of the monotonous changes in the liquidus temperatures caused by the increase in the Ti content in $(Mo_{0.25}Nb_{0.25}Ta_{0.25}Zr_{0.25})_{100-x}Ti_x$, that of the Nb content in $(Ti_{0.25}Mo_{0.25}Ta_{0.25}Zr_{0.25})_{100-x}Nb_x$, that of the Ta content in $(Ti_{0.25}Nb_{0.25}Mo_{0.25}Zr_{0.25})_{100-x}Ta_x$, that of the Zr content in $(Ti_{0.25}Nb_{0.25}Ta_{0.25}Mo_{0.25})_{100-x}Zr_x$, and that of the Mo content in $(Ti_{0.25}Nb_{0.25}Ta_{0.25}Zr_{0.25})_{100-x}Mo_x$.

Fig. 5 shows the temperature dependence of the distribution coefficient ($k = C_S/C_L$, where C_S and C_L are the compositions of the solid and liquid phases, respectively) in the solidification of equiatomic TiNbTaZrMo ($Ti_{20}Nb_{20}Ta_{20}Zr_{20}Mo_{20}$), estimated based on the thermodynamic calculations considering a single bcc phase

Table 2
Composition analysis results of equiatomic TiNbTaZrMo ($Ti_{20}Nb_{20}Ta_{20}Zr_{20}Mo_{20}$) HEA from EPMA-WDS: (a) as-cast and (b) annealed at 1273 K for 168 h.

Region	Ti	Nb	Ta	Zr	Mo
(a) As-cast					
A (Dendrite)	15.5	22.4	30.8	8.4	22.9
B (Int.-Dend.)	24.7	13.6	7.7	40.9	13.1
(b) Annealed					
C	15.8	23.4	27.5	7.5	25.8
D	22.1	22.9	20.5	8.3	26.1
E	22.4	22.0	18.1	12.4	25.1
F	22.3	11.3	3.6	55.3	7.4

Table 3
Lattice constants of bcc solid-solution phase estimated using Vegard's law in equiatomic TiNbTaZrMo ($Ti_{20}Nb_{20}Ta_{20}Zr_{20}Mo_{20}$) HEA based on the experimental analysis results: (a) as-cast and (b) annealed at 1273 K for 168 h.

Resions	Estimated lattice constants [nm]
(a) As-cast	
A (Dendrite)	0.328
B (Int.-Dend.)	0.338
(b) Annealed	
C	0.327
D	0.327
E	0.328
F	0.343

and a single liquid phase. The effective distribution coefficients (k_e), defined as the k at the liquidus temperature of equiatomic TiNbTaZrMo ($Ti_{20}Nb_{20}Ta_{20}Zr_{20}Mo_{20}$), were as follows: $k_{e-Ti} = 0.69$, $k_{e-Nb} = 1.20$, $k_{e-Ta} = 1.50$, $k_{e-Zr} = 0.75$, and $k_{e-Mo} = 1.38$. The values of k for Ti and Zr are lower than 1, indicating that these elements are expelled from the bcc solid-solution phase to the residual liquid phase, resulting in the enrichment of the final transient region. On the other hand, the values of k for Ta, Nb, and Mo were higher than 1; this means that these elements were abundant in the bcc solid-solution phase during solidification. The enrichment in Ti and Zr of the inter-dendrite region in the as-cast equiatomic TiNbTaZrMo HEA (Fig. 3 and Table 2) can be explained through the values of the distribution coefficients obtained from the thermodynamic calculations.

4. Discussion

Two bcc solid-solution phases were observed in the as-cast equiatomic TiNbTaZrMo ($Ti_{20}Nb_{20}Ta_{20}Zr_{20}Mo_{20}$). In the annealed equiatomic TiNbTaZrMo ($Ti_{20}Nb_{20}Ta_{20}Zr_{20}Mo_{20}$), the main constituent phases were the coarse dendrite phase (regions C and D in Figs. 2 and 3), with a bcc structure, and the inter-dendrite region (region F in Figs. 2 and 3), also with a bcc structure. In the present work, the mechanism of the dual bcc phase formation is discussed, based on two possible mechanisms: the first is segregation during solidification, and the second is decomposition of the single bcc phase due to the miscibility gap of the bcc phases. The first one, which involves solidification, was discussed in section 3 above, and the second one, which involves decomposition, will be described in the following paragraphs. The phase diagrams of Ti-Nb-Ta-Mo-V-W HEAs with bcc structures have been reported in the literature [5], and the miscibility gap between the bcc solid-solution phase, i.e., the phase separation of the single bcc solid-solution phase to two bcc solid-solution phases (bcc1 + bcc2), has been shown in pseudo-binary TaMoW-V, NbTaMoW-V, and TiNbTaMoW-V alloy systems. Fig. 6 shows the mixing enthalpy map (a) and the existence of the miscibility gap of the bcc phase in the thermodynamic binary phase diagram (b). The values of the mixing enthalpy in binary i-j systems (ΔH_{ij}) [kJ/mol] were obtained from the literature [17]. Most of the binary phase diagrams [18–30] were investigated using the National Institute for Materials Science (NIMS) AtomWork Database [18]. The values of ΔH_{ij} for the elemental pairs Ti-Nb (+2), Ti-Ta (+1), Nb-Zr (+4), and Ta-Zr (+3) are positive, implying the decomposition of the bcc solid-solution phase to separated bcc phases. Among the binary phase diagrams featuring Ti, Nb, Ta, Zr, and Mo, miscibility gaps of the bcc solid-solution phase were reported for Ti-Mo [22,23], Nb-Zr [26], and Ta-Zr [28] alloy systems. These reports, concerning the decomposition of bcc phases in Ti-Nb-Ta-Mo-V-W HEAs [5] and binary Ti-Mo, Nb-Zr, and Ta-Zr alloys (Fig. 6), imply the possibility of the formation of a dual bcc phase owing to the miscibility gap of the bcc solid-solution phase in Ti-Nb-Ta-Zr-Mo HEAs. This was investigated using thermodynamic calculations.

Fig. 7 shows pseudo-binary phase diagrams focusing on the phase separation of the bcc solid-solution phases in Ti-Nb-Ta-Zr-Mo alloys and Ti-Zr-Nb-Ta alloys estimated based on thermodynamic calculations considering single and separated bcc phases: (a) MoNbTaZr-Ti, (b) TiMoTaZr-Nb, (c) TiNbMoZr-Ta, (d) TiNbTaMo-Zr, (e) TiNbTaZr-Mo, and (f) NbTa-TiZr. The pseudo-binary phase diagrams in Fig. 7 were constructed using only the Gibbs free energies of the single and dual bcc phases; thus, the thermal equilibrium state cannot be discussed using Fig. 7. One can notice the existence of a miscibility gap for the bcc solid-solution phase in the Ti-Nb-Ta-Zr-Mo alloys (Fig. 7a to e) and Ti-Nb-Ta-Zr alloy (Fig. 7f). The maximum temperature of the miscibility gap of equiatomic TiNbTaZrMo ($Ti_{20}Nb_{20}Ta_{20}Zr_{20}Mo_{20}$) was estimated to be 898 K (Fig. 7a and e); this value is higher than that of the quaternary Ti-Nb-Ta-Zr alloys (599 K) (Fig. 7f). The maximum temperature of the miscibility gap of the bcc solid-solution phase increases with increases in the Nb and Zr contents in equiatomic TiNbTaZrMo ($Ti_{20}Nb_{20}Ta_{20}Zr_{20}Mo_{20}$) (Fig. 7b and d). On the other hand, increases in the Ta and Mo contents in equiatomic TiNbTaZrMo ($Ti_{20}Nb_{20}Ta_{20}Zr_{20}Mo_{20}$) lead to decreases in the maximum temperature of the miscibility gap of the bcc solid-solution phase (Fig. 7c and e). Table 4 shows the equilibrium compositions of the separated bcc phases in the equiatomic TiNbTaZr ($Ti_{25}Nb_{25}Ta_{25}Zr_{25}$) alloy (a) and equiatomic TiNbTaZrMo ($Ti_{20}Nb_{20}Ta_{20}Zr_{20}Mo_{20}$) (b), which were estimated based on thermodynamic calculations considering a single bcc phase and separated bcc phases. In the equiatomic TiNbTaZr ($Ti_{25}Nb_{25}Ta_{25}Zr_{25}$) alloy (Table 4a), Nb- and Ta-rich (b.c.c.-1) and Ti- and Zr-rich (b.c.c.-2) bcc phases were formed through phase separation of the single bcc phase. The phase separation of the single bcc solid-solution phase in equiatomic TiNbTaZrMo ($Ti_{20}Nb_{20}Ta_{20}Zr_{20}Mo_{20}$) led to the formation of Ti-, Ta-, and Zr-rich b.c.c.-1 and Nb- and Mo-rich b.c.c.-2 phases. The distributions of Ta in the equiatomic TiNbTaZr ($Ti_{25}Nb_{25}Ta_{25}Zr_{25}$) alloy (Table 4a) and equiatomic TiNbTaZrMo ($Ti_{20}Nb_{20}Ta_{20}Zr_{20}Mo_{20}$) (Table 4b) are different; Ta is concentrated in the Nb-rich phase (b.c.c.-1) in the quaternary equiatomic TiNbTaZr ($Ti_{25}Nb_{25}Ta_{25}Zr_{25}$) alloy, while it is concentrated in the Ti-Zr-enriched phase (b.c.c.-1) in equiatomic TiNbTaZrMo ($Ti_{20}Nb_{20}Ta_{20}Zr_{20}Mo_{20}$). The addition of Mo to the equiatomic TiNbTaZr ($Ti_{25}Nb_{25}Ta_{25}Zr_{25}$) alloy affects the distribution of the constituent elements during the decomposition of the bcc phase. The thermodynamic calculations suggest a miscibility gap of the bcc phase in Ti-Nb-Ta-Zr-Mo alloys; however, the elemental distribution of as-cast and annealed equiatomic TiNbTaZrMo ($Ti_{20}Nb_{20}Ta_{20}Zr_{20}Mo_{20}$) cannot be explained through the miscibility gap of the bcc phase. The annealing temperature in the present study (1273 K) is much higher than the maximum temperature of the miscibility gap of the bcc phase in equiatomic TiNbTaZrMo ($Ti_{20}Nb_{20}Ta_{20}Zr_{20}Mo_{20}$). Therefore, the formation of dual bcc phases via miscibility-gap-induced decomposition of the bcc phase is unfavorable in equiatomic TiNbTaZrMo

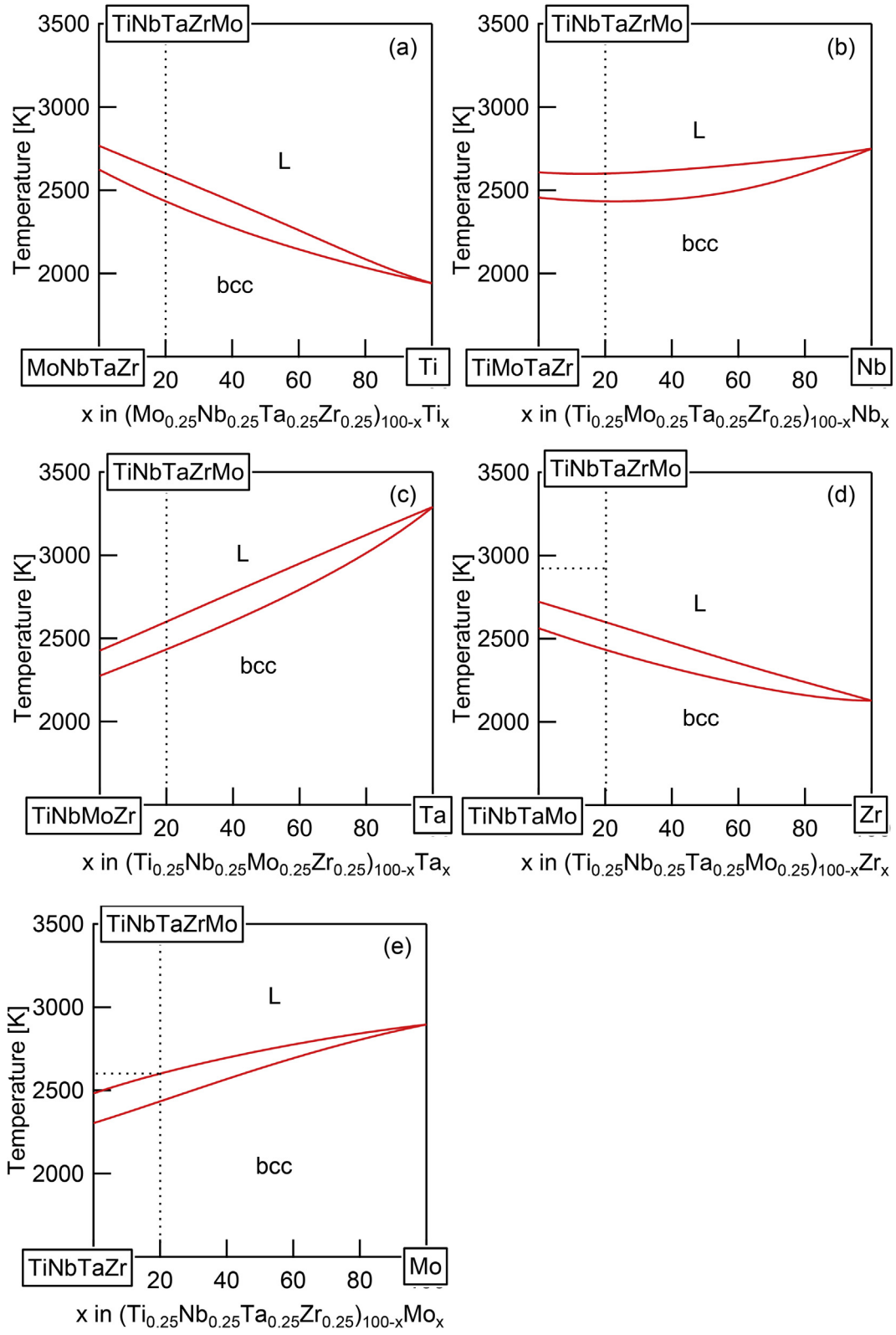

Fig. 4. Pseudo-binary phase diagrams focusing on liquidus and solidus temperatures of Ti-Nb-Ta-Zr-Mo alloys estimated from thermodynamic calculations considering a single bcc phase and single liquid phase: (a) MoNbTaZr-Ti, (b) TiMoTaZr-Nb, (c) TiNbMoZr-Ta, (d) TiNbTaMo-Zr, and (e) TiNbTaZr-Mo.

($Ti_{20}Nb_{20}Ta_{20}Zr_{20}Mo_{20}$) and was not observed in the present study, even after annealing at 1273 K. DSC may enable the investigation of the decomposition of the bcc phase of equiatomic TiNbTaZrMo ($Ti_{20}Nb_{20}Ta_{20}Zr_{20}Mo_{20}$). The DSC curve of equiatomic TiNbTaZrMo ($Ti_{20}Nb_{20}Ta_{20}Zr_{20}Mo_{20}$) is shown in Fig. S2 in the supplementary material; heat release due to structural changes was not detected

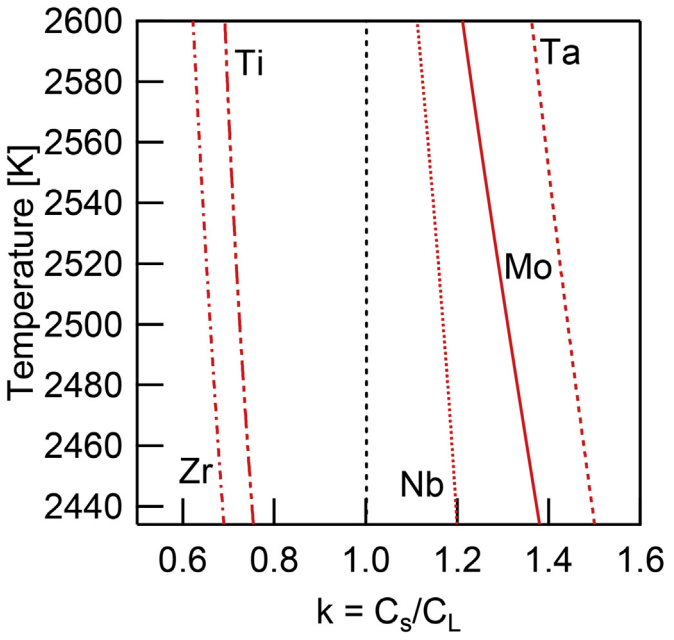

Fig. 5. Temperature dependence of the distribution coefficient ($k = C_s/C_L$) for the solidification of equiatomic TiNbTaZrMo ($Ti_{20}Nb_{20}Ta_{20}Zr_{20}Mo_{20}$) HEA estimated based on thermodynamic calculations considering a single bcc phase and single liquid phase.

(a) ΔH_{ij} map

	Ti	Nb	Ta	Zr	Mo
Ti		2	1	0	-4
Nb			0	4	-6
Ta				3	-5
Zr					-6
Mo					

(b) bcc phase separation

	Ti	Nb	Ta	Zr	Mo
Ti					O
Nb				O	
Ta				O	
Zr					
Mo					

Fig. 6. (a) Mixing enthalpy map for binary i-j system (ΔH_{ij}) and (b) bcc phase separation in the thermodynamic binary phase diagram.

during annealing at 1023 K. Thus, the heat released by the annealing-induced structural change was insufficient to affect the DSC measurements. Consequently, the formation of dual bcc phases in equiatomic TiNbTaZrMo ($Ti_{20}Nb_{20}Ta_{20}Zr_{20}Mo_{20}$) cannot be explained through the decomposition of the bcc phase owing to the miscibility gap of the bcc phases; instead, segregation during solidification is the dominant cause of the formation of dual bcc phases in equiatomic TiNbTaZrMo ($Ti_{20}Nb_{20}Ta_{20}Zr_{20}Mo_{20}$).

Equiatomic TiNbTaZrMo ($Ti_{20}Nb_{20}Ta_{20}Zr_{20}Mo_{20}$) shows superior mechanical properties and biocompatibility [8]. However, the significantly high liquidus temperatures suggest that there are limitations to using this new biomaterial, and they are associated with difficulties in the fabrication processes. Reducing the liquidus temperature of this alloy is important for the further development of Ti-Nb-Ta-Zr-Mo HEAs. The present study showed that thermodynamic calculations are effective for evaluating the microstructure formation process of equiatomic TiNbTaZrMo ($Ti_{20}Nb_{20}Ta_{20}Zr_{20}Mo_{20}$) during solidification. This indicates that new non-equiatomic Ti-Nb-Ta-Zr-Mo HEAs can be designed based on the thermodynamic calculations by focusing on liquidus and solidus temperatures and the value of k (or k_e). In the following section, we discuss the design of non-equiatomic Ti-Nb-Ta-Zr-Mo HEAs by utilizing thermodynamic calculations. The value of m_L is important when discussing the compositional dependence on the liquidus temperature. According to the thermodynamic calculations, increases in the Ti and Zr contents in Ti-Nb-Ta-Zr-Mo HEAs lead to decreases in the liquidus temperature, and decreases in the contents of high-melting-temperature elements—Ta and Mo—lead to decreases in the liquidus temperature as well. To obtain non-equiatomic Ti-Nb-Ta-Zr-Mo HEAs whose liquidus temperatures are lower than that of equiatomic TiNbTaZrMo ($Ti_{20}Nb_{20}Ta_{20}Zr_{20}Mo_{20}$), the liquidus temperatures of non-equiatomic Ti_{x1}NbTaZrMo, TiNbTa_{x2}ZrMo, TiNbTaZr_{x1}Mo, and TiNbTaZrMo_{x2} ($x1 > 1, x2 < 1$) alloys were considered. First, the values of x1 and x2 were evaluated to satisfy the condition on mixing entropy, $\Delta S_{mix} \geq 1.5\,R$ (R is the gas constant), in accordance with the entropy-based definition of HEAs [5,6]. This gives $x1 = 2.6$ and $x2 = 0.2$. The ΔS_{mix} value of non-equiatomic $Ti_{2.6}$NbTaZrMo ($Ti_{39.4}Nb_{15.2}Ta_{15.2}Zr_{15.2}Mo_{15.2}$), non-equiatomic TiNb$Ta_{0.2}$ZrMo ($Ti_{23.8}Nb_{23.8}Ta_{4.8}Zr_{23.8}Mo_{23.8}$), non-equiatomic TiNbTa$Zr_{2.6}$Mo ($Ti_{15.2}Nb_{15.2}Ta_{15.2}Zr_{39.4}Mo_{15.2}$), and non-equiatomic TiNbTaZr$Mo_{0.2}$ ($Ti_{23.8}Nb_{23.8}Ta_{23.8}Zr_{23.8}Mo_{4.8}$) was 1.51 R. The calculated liquidus temperatures T_L are shown in Table 5a, together with the various empirical parameters (mixing enthalpy ΔH_{mix}, δ, and Ω parameters) for HEAs. The empirical parameters of Ti-Nb-Ta-Zr-Mo HEAs are explained in detail in a previous paper [8]. The ΔH_{mix}, δ, and Ω parameters for non-equiatomic Ti-Nb-Ta-Zr-Mo HEAs indicate high solid-solution phase formation tendencies in non-equiatomic $Ti_{2.6}$NbTaZrMo ($Ti_{39.4}Nb_{15.2}Ta_{15.2}Zr_{15.2}Mo_{15.2}$), non-equiatomic TiNb$Ta_{0.2}$ZrMo ($Ti_{23.8}Nb_{23.8}Ta_{4.8}Zr_{23.8}Mo_{23.8}$), and non-equiatomic TiNbTaZr$Mo_{0.2}$ ($Ti_{23.8}Nb_{23.8}Ta_{23.8}Zr_{23.8}Mo_{4.8}$) alloys. The liquidus temperatures of the non-equiatomic $Ti_{2.6}$NbTaZrMo ($Ti_{39.4}Nb_{15.2}Ta_{15.2}Zr_{15.2}Mo_{15.2}$) alloy was the lowest among those of the Ti-Nb-Ta-Zr-Mo alloys, as shown in Table 5a. Table 5b shows the value of k_e for the non-equiatomic $Ti_{2.6}$NbTaZrMo ($Ti_{39.4}Nb_{15.2}Ta_{15.2}Zr_{15.2}Mo_{15.2}$) alloy. The enrichment in Ti and Zr in the interdendrite region during the solidification of the alloy was predicted. Based on the empirical parameters and thermodynamic calculation results, an ingot of the non-equiatomic $Ti_{2.6}$NbTaZrMo ($Ti_{39.4}Nb_{15.2}Ta_{15.2}Zr_{15.2}Mo_{15.2}$) alloy was fabricated and the solidification microstructure was investigated to test the new Ti-Nb-Ta-Zr-Mo HEA design technique.

Fig. 8 shows the microstructure analysis results for the arc-melted ingot of the non-equiatomic $Ti_{2.6}$NbTaZrMo ($Ti_{39.4}Nb_{15.2}Ta_{15.2}Zr_{15.2}Mo_{15.2}$) HEA. The XRD pattern (Fig. 8a) shows the formation of a bcc phase. The SEM-BSE image (Fig. 8b) shows the equiatomic dendrite structure composed of a white-gray-contrast dendrite phase and dark-gray-contrast inter-dendrite phases. The EPMA-WDS elemental mapping (Fig. 8c) shows the formation of a

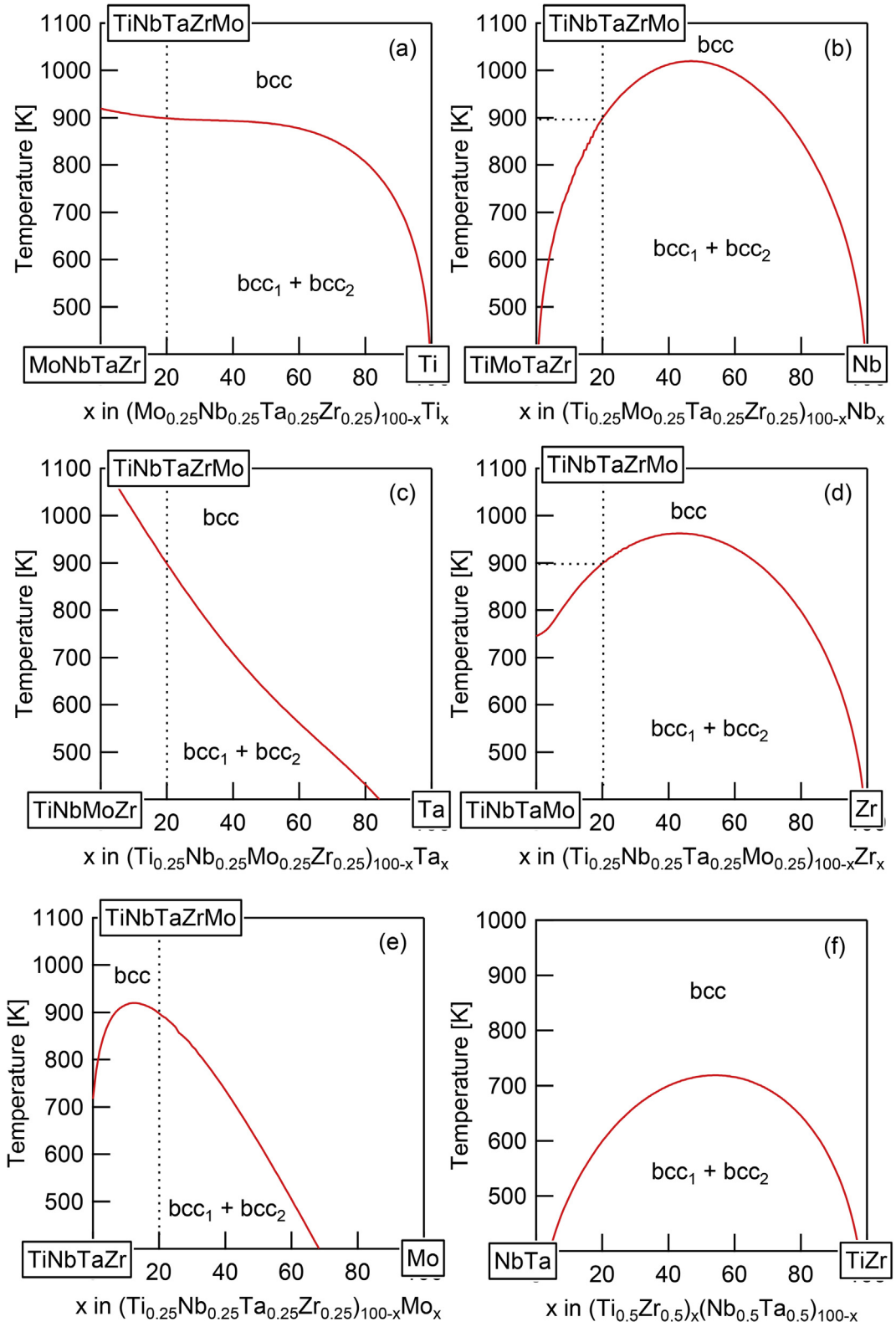

Fig. 7. Pseudo-binary phase diagrams focusing on phase separation of the bcc solid-solution phase in Ti-Nb-Ta-Zr-Mo and Ti-Nb-Ta-Zr alloys estimated from thermodynamic calculations considering a single bcc phase and separated bcc phases: (a) MoNbTaZr-Ti, (b) TiMoTaZr-Nb, (c) TiNbMoZr-Ta, (d) TiNbTaMo-Zr, (e) TiNbTaZr-Mo, (f) NbTa-TiZr.

Ta- and Mo-rich dendrite phase and a Ti- and Zr-enriched inter-dendrite phase. The composition analysis results (Fig. 8d) show Nb, Ta, and Mo enrichment in the dendrite regions, and the formation of Ti- and Zr-rich inter-dendrite regions. The distribution of the constituent elements in the as-cast specimen is in agreement with the thermodynamic calculation results of k_e (Table 5b). The lattice constants of the dendrite and inter-dendrite phases, which were estimated using Vegard's law [16] and the EPMA-WDS analysis

Table 4
Equilibrium compositions of the separated bcc phases in (a) equiatomic TiNbTaZr ($Ti_{25}Nb_{25}Ta_{25}Zr_{25}$) alloy and (b) equiatomic TiNbTaZrMo ($Ti_{20}Nb_{20}Ta_{20}Zr_{20}Mo_{20}$) HEA estimated based on thermodynamic calculations considering a single bcc phase and the separated bcc phases.

(a) TiNbTaZr

Temp. [k]	Ti	Nb	Ta	Zr
b.c.c.-1				
300	0.4	51.5	47.2	0.9
500	3.7	52.9	39.6	3.8
700	14.0	43.3	30.4	12.3
b.c.c.-2				
300	48.1	0.2	4.2	47.5
500	41.1	3.9	14.0	41.1
700	27.3	21.1	23.9	27.7

(b) TiNbTaZrMo

Temp. [k]	Ti	Nb	Ta	Zr	Mo
b.c.c.-1					
300	33.1	0.0	31.6	33.2	2.1
500	32.5	1.1	27.8	33.1	5.6
700	29.5	5.4	24.1	30.8	10.3
800	26.4	9.9	22.4	27.7	13.6
b.c.c.-2					
300	0.1	50.3	2.4	0.0	47.2
500	1.4	48.3	8.4	0.5	41.5
700	5.0	43.1	13.5	2.9	35.4
800	8.3	38.5	15.6	5.9	31.6

Table 5
Alloy design of non-equiatomic Ti-Nb-Ta-Zr-Mo HEAs. (a) Empirical alloy parameters for solid-solution phase formation in HEAs and the calculated liquidus temperatures of equiatomic TiNbTaZrMo ($Ti_{20}Nb_{20}Ta_{20}Zr_{20}Mo_{20}$), non-equiatomic $Ti_{2.6}$NbTaZrMo ($Ti_{39.4}Nb_{15.2}Ta_{15.2}Zr_{15.2}Mo_{15.2}$), non-equiatomic $TiNbTa_{0.2}$ZrMo ($Ti_{23.8}Nb_{23.8}Ta_{4.8}Zr_{23.8}Mo_{23.8}$), non-equiatomic $TiNbTaZr_{2.6}$Mo ($Ti_{15.2}Nb_{15.2}Ta_{15.2}Zr_{39.4}Mo_{15.2}$), and non-equiatomic $TiNbTaZrMo_{0.2}$ ($Ti_{23.8}Nb_{23.8}Ta_{23.8}Zr_{23.8}Mo_{4.8}$) HEAs. (b) Thermodynamic calculation results for the effective distribution coefficient of non-equiatomic $Ti_{2.6}$NbTaZrMo ($Ti_{39.4}Nb_{15.2}Ta_{15.2}Zr_{15.2}Mo_{15.2}$).

(a) Alloy parameters

Alloys	ΔH_{mix} [kJ/mol]	δ [%]	Ω	T_L [K]
TiNbTaZrMo	−1.8	5.9	19.7	2600
$Ti_{2.6}$NbTaZrMo	−1.2	5.2	26.4	2441
$TiNbTa_{0.2}$ZrMo	−2.3	6.4	13.4	2468
$TiNbTaZr_{2.6}$Mo	−0.9	6.8	36.1	2481
$TiNbTaZrMo_{0.2}$	1.3	5.5	24.2	2497

(b) k_e in $Ti_{2.6}$NbTaZrMo

Ti	Nb	Ta	Zr	Mo
0.61	1.06	1.30	0.70	1.12

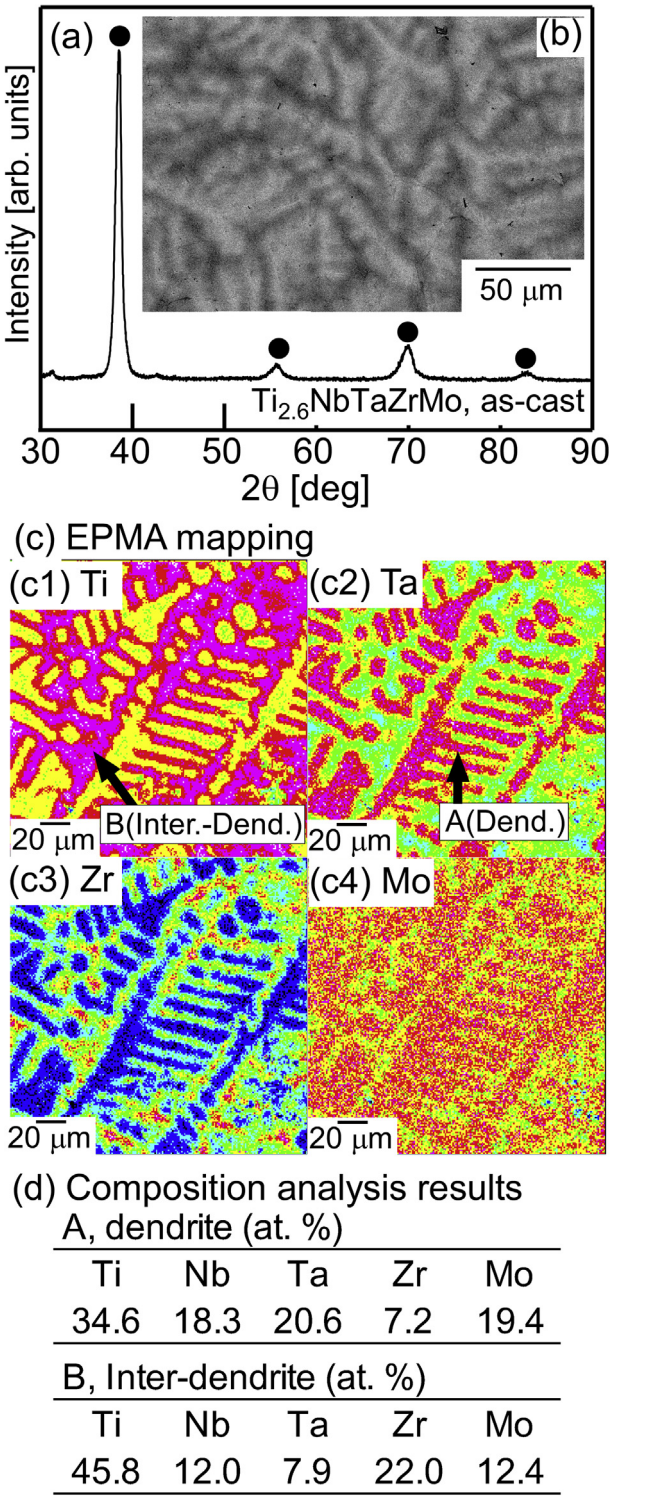

Fig. 8. Microstructure analysis results for as-cast non-equiatomic $Ti_{2.6}$NbTaZrMo ($Ti_{39.4}Nb_{15.2}Ta_{15.2}Zr_{15.2}Mo_{15.2}$) HEA: (a) XRD pattern, (b) SEM-BSE image, (c) EPMA elemental map, and (d) compositions of dendrite and inter-dendrite regions in the as-cast specimen from EPMA-WDS.

results, were 0.328 and 0.332 nm, respectively. The difference between the lattice constants of the dendrite and inter-dendrite phases in the as-cast non-equiatomic $Ti_{2.6}$NbTaZrMo ($Ti_{39.4}Nb_{15.2}Ta_{15.2}Zr_{15.2}Mo_{15.2}$) HEA (0.328 and 0.332 nm) was much smaller than that for equiatomic TiNbTaZrMo ($Ti_{20}Nb_{20}Ta_{20}Zr_{20}Mo_{20}$) (0.328 and 0.338 nm, Table 2a), resulting in the appearance of single bcc peaks in the XRD pattern of the non-equiatomic $Ti_{2.6}$NbTaZrMo ($Ti_{39.4}Nb_{15.2}Ta_{15.2}Zr_{15.2}Mo_{15.2}$) alloy (Fig. 8a). These results indicate that the thermodynamic calculations focusing on the solidification were effective not only for the evaluation of the solidification microstructure, but also for the design of Ti-Nb-Ta-Zr-Mo HEAs. The compositional dependence on the microstructure and constituent phases in non-equiatomic Ti-Nb-Ta-Zr-Mo HEAs, which were designed by combining empirical parameters for HEAs and thermodynamic calculations, will be reported in greater detail in future papers, along with experimental data on the mechanical properties and biocompatibility.

5. Conclusions

The microstructures of equiatomic TiNbTaZrMo

($Ti_{20}Nb_{20}Ta_{20}Zr_{20}Mo_{20}$) HEAs for metallic biomaterials were investigated and discussed based on thermodynamic calculation results. Non-equiatomic $Ti_{2.6}NbTaZrMo$ ($Ti_{39.4}Nb_{15.2}Ta_{15.2}Zr_{15.2}Mo_{15.2}$) HEA was designed based on thermodynamic calculations by focusing on solidification. The following conclusions could be drawn based on the results of our study:

(1) The as-cast specimens had equiaxial dendrite structures. Ta, Nb, and Mo were abundant in the main dendrite phase with a bcc structure, while Ti and Zr showed the tendency to be abundant in the inter-dendrite region with a bcc structure in the equiatomic TiNbTaZrMo ($Ti_{20}Nb_{20}Ta_{20}Zr_{20}Mo_{20}$) and non-equiatomic $Ti_{2.6}NbTaZrMo$ ($Ti_{39.4}Nb_{15.2}Ta_{15.2}Zr_{15.2}Mo_{15.2}$) HEAs. The distribution of the constituent elements in the as-cast specimens can be explained through the distribution coefficients during solidification, which was evaluated using thermodynamic calculations.
(2) The liquidus and solidus temperatures of equiatomic TiNbTaZrMo ($Ti_{20}Nb_{20}Ta_{20}Zr_{20}Mo_{20}$) were estimated to be 2600 and 2433 K, respectively. Increases in the Ti and Zr contents and decreases in the Ta and Mo contents are predicted to decrease the liquidus and solidus temperatures in Ti-Nb-Ta-Zr-Mo alloys.
(3) Annealing leads to the coarsening of the Ta-Nb-Mo-rich bcc phase and the enhancement of the segregation of Zr in the inter-dendrite region in equiatomic TiNbTaZrMo ($Ti_{20}Nb_{20}Ta_{20}Zr_{20}Mo_{20}$).
(4) Thermodynamic calculations focusing on the solidification (i.e., liquidus and solidus temperatures and the distribution coefficient) were applied to the design of Ti-Nb-Ta-Zr-Mo HEAs. A non-equiatomic $Ti_{2.6}NbTaZrMo$ ($Ti_{39.4}Nb_{15.2}Ta_{15.2}Zr_{15.2}Mo_{15.2}$) HEA was designed and the solidification microstructure was clarified.

Acknowledgements

This work was partially supported by JSPS KAKENHI [grant number 18H03844, 18K04750, 25220912], the Council for Science, Technology and Innovation, Cross-Ministerial Strategic Innovation Promotion Program (SIP), Innovative Design/Manufacturing Technologies (Establishment and Validation of the Base for 3D Design & Additive Manufacturing Standing on the Concepts of “Anisotropy” & “Customization”) of the New Energy and Industrial Technology Development Organization (NEDO), and by scientific grants from the Hitachi Metals-Materials Science Foundation. The authors are grateful to Prof. T. Tanaka and Prof. M. Suzuki at Osaka University for their help with the thermodynamic calculations.

Appendix A. Supplementary data

Supplementary data related to this article can be found at https://doi.org/10.1016/j.jallcom.2018.04.082.

References

[1] B. Cantor, I.T.H. Chang, P. Knight, A.J.B. Vincent, Microstructural development in equiatomic multicomponent alloys, Mater. Sci. Eng., A 375–377 (2004) 213–218.
[2] J.W. Yeh, S.K. Chen, S.J. Lin, J.Y. Gan, T.S. Chin, T.T. Shun, C.H. Tsau, S.Y. Chang, Nanostructured high-entropy alloys with multiple principal elements: novel alloy design concepts and outcomes, Adv. Eng. Mater. 6 (2004) 299–303.
[3] S. Ranganathan, Alloyed pleasures: multimetallic cocktails, Curr. Sci. 85 (2003) 1404–1406.
[4] Y. Zhang, Y.J. Zhou, J.P. Lin, G.L. Chen, P.K. Liew, Solid-solution phase formation rules for multi-component alloys, Adv. Eng. Mater. 10 (2008) 534–538.
[5] B.S. Murty, J.-W. Yeh, S. Ranganathan, High-entropy Alloys, first ed., Elsevier, 2014.
[6] M.C. Gao, J.-W. Yeh, P.K. Liaw, Y. Zhang, High-entropy Alloys, Fundamentals and Applications, first ed., Springer, 2016.
[7] W. Zhang, P.K. Liew, Y. Zhang, Science and technology in high-entropy alloys, Sci. China Mater 61 (2018) 2–22.
[8] M. Todai, T. Nagase, T. Hori, A. Matsugaki, A. Sekita, T. Nakano, Novel TiNbTaZrMo high-entropy alloys for metallic biomaterials, Scripta Mater. 129 (2017) 65–68.
[9] S.P. Wang, J. Xu, TiZrNbTaMo high-entropy alloy designed for orthopedic implants: as-cast microstructure and mechanical properties, Mater. Sci. Eng. C 73 (2017) 80–89.
[10] Mitsuwa Chemical Co., Ltd., Japan, http://www.eonet.ne.jp/~mitsuwa-chem/index.html.
[11] The Nilaco Co. Ltd., Japan, http://nilaco.jp/en/index.php.
[12] Rare Metallic Co., Ltd., Japan, http://rare-meta.co.jp/.
[13] Osaka Asahi Co., Ltd., Japan, http://www.osaka-asahi.com/.
[14] T. Nagase, M. Matsumoto, Y. Fujii, Microstructure of Ti-Ag immiscible alloys with metastable liquid phase separation, J. Alloys Compd. 738 (2018) 440–447.
[15] C.W. Bale, A.D. Pelton, W.T. Thompson, G. Eriksson, FactSage®, Ecole Polytechnique, Montreal, 2001, 2016, http://www.crct.polymtl.ca. (Accessed 26 October 2016).
[16] L. Vegard, Die Konstitution der Mischkristalle und die Raumfüllung der Atome, Zeitschrift fur Physik 5 (1921) 17–26 (in German).
[17] A. Takeuchi, A. Inoue, Classification of bulk metallic glasses by atomic size difference, heat of mixing and period of constituent elements and its application to characterization of the main alloying element, Mater. Trans. 46 (2005) 2817–2829.
[18] Y. Xu, M. Yamazaki, P. Villars, Inorganic materials database for exploring the nature of material, Jpn. J. Appl. Phys. 50 (2011), 11RH02 1–5.
[19] T.B. Massalski (Ed.), Nb-Ti, Binary Alloy Phase Diagrams, 1990, pp. 2775–2778.
[20] L. Kaufman, Coupled thermochemical and phase diagram data for tantalum based binary alloys, Calphad 15 (1991) 243–259.
[21] K.C. Hari Kumar, P. Wollants, L. Delacy, Thermodynamic assessment of the Ti-Zr system and calculation of the Nb-Ti-Zr phase, J. Alloys Compd. 206 (1994) 121–127.
[22] T.B. Massalski (Ed.), Mo-Ti, Binary Alloy Phase Diagrams, 1990, pp. 2675–2679.
[23] G. Rubin, A. Finel, Application of first-principles methods to binary and ternary alloy phase diagram predictions, J. Phys. Condens. Mater 7 (1995) 3139–3152.
[24] T.B. Massalski (Ed.), Nb-Ta, Binary Alloy Phase Diagrams, 1990, pp. 2772–2773.
[25] C. Ravi, B.K. Panigrahi, M.C. Valsakumar, A. Van de Walle, First-principles calculation of phase equilibrium of V-Nb, V-Ta, and Nb-Ta alloys, Phys. Rev. B 85 (2012), 054202, 1–10.
[26] A. Fernandez Guillermet, Thermodynamic analysis of the stable phases in the Zr-Nb system and calculation of the phase diagram, Z. Metallkd 82 (1991) 478–487.
[27] T.B. Massalski (Ed.), Mo-Nb, Binary Alloy Phase Diagrams, 1990, pp. 2631–2634.
[28] T.B. Massalski (Ed.), Ta-Zr, Binary Alloy Phase Diagrams, 1990, pp. 3441–3443.
[29] T.B. Massalski (Ed.), Mo-Ta, Binary Alloy Phase Diagrams, 1990, pp. 2671–2672.
[30] T.B. Massalski (Ed.), Mo-Zr, Binary Alloy Phase Diagrams, 1990, pp. 2690–2691.